

1 FAULT SLIP POTENTIAL NEAR THE DEADLY M_w 6.8 AL HAOUZ, MOROCCO EARTHQUAKE

2 Will Levandowski, Tetra Tech, Inc.

3 Will.Levandowski@tetratech.com

5 Abstract

6 Thousands were killed by the September 8, 2023, M_w 6.8 Al Haouz, Morocco earthquake in the Western High
7 Atlas. To identify the faults and fault orientations most likely to host aftershocks and future large earthquakes,
8 regional crustal stress is estimated from focal mechanism inversions, and the associated slip potential of known
9 and suspected active faults is modeled. North-south shortening is accommodated by a mix of reverse, oblique-
10 reverse, and strike-slip motion. As such, many fault orientations are well aligned for slip—steep NNE-, SSW-,
11 SE-, or NW-striking planes, gently (~ 15 – 50°) dipping east- and west-striking planes, and all orientations
12 between— and nearly all previously identified active faults have high slip potential. By contrast, steep E–W and
13 nearly all N–S faults may be relatively stable.

15 Introduction

16 Following a major earthquake, quickly characterizing the regional crustal stress field can lend insight into
17 the fault populations most likely to host aftershocks and future mainshocks. The 8 September 2023 M_w 6.8 Al
18 Haouz, Morocco earthquake killed nearly 3,000 people in an area of the Western High Atlas (WHA) mountains
19 (**Figure 1**) with sparse stress constraints. It is the deadliest in Morocco since the 1960 M 5.9 in Agadir, 140 km
20 southwest along the WHA. Here, the limited regional stress data—focal mechanisms from prior earthquakes in
21 the WHA, central High Atlas (CHA) and High/Middle Atlas junction (HMAJ) area—are compiled and inverted to
22 examine regional stress and associated fault slip potential.

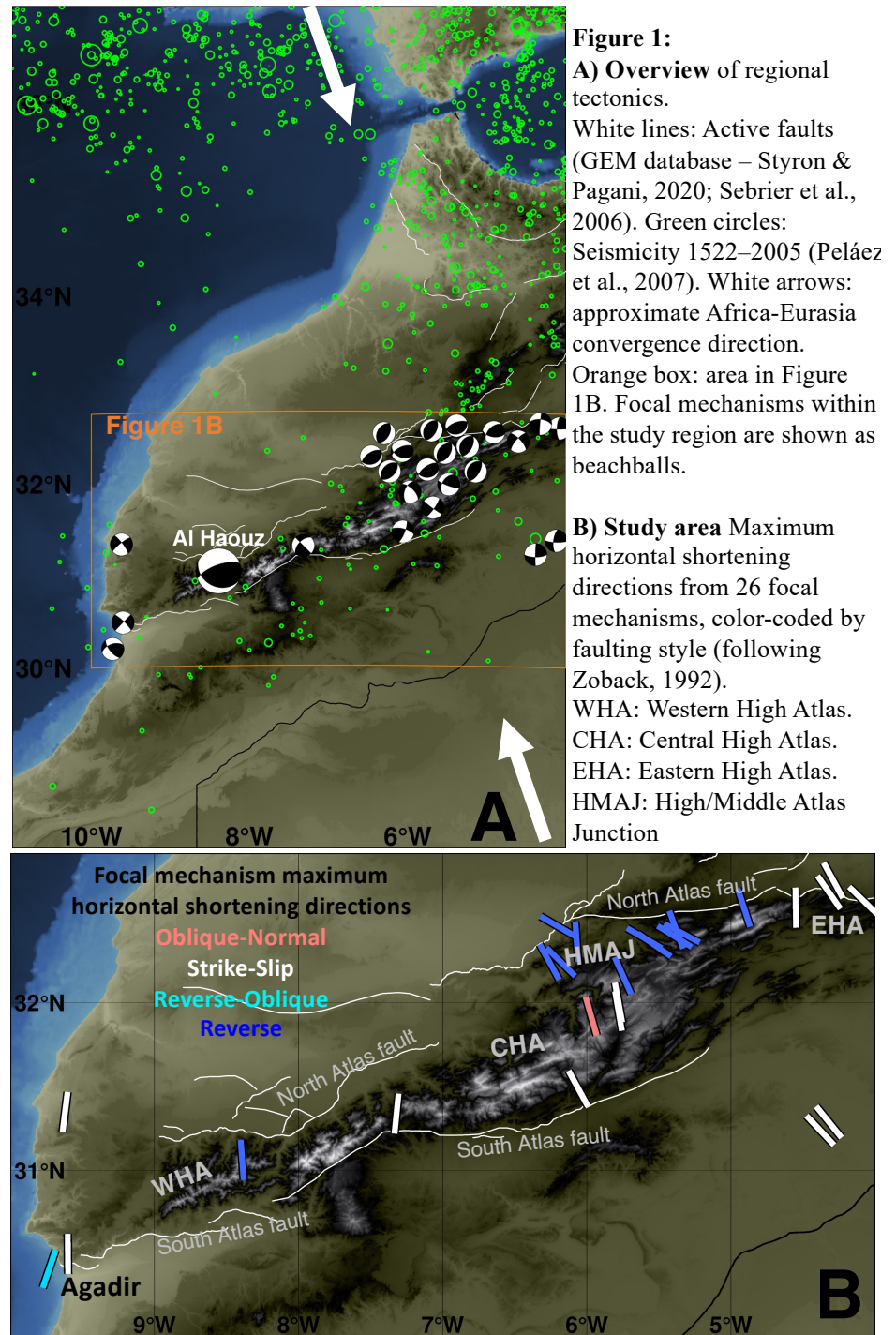
23 Six moment tensors available for the Haouz mainshock (see Data and Resources) indicate reverse to
24 reverse-oblique slip with median nodal plane strike/dip $255/70^\circ$ and $125/30^\circ$ (250 – $261/68$ – 73° and 116 – $136/23$ –
25 37° ; dip directions are 90° clockwise of strike). Finite fault modeling finds better fit to InSAR and teleseismic

26 waveforms with the WSW-
 27 striking plane. Hypocentral
 28 depths range from 23 to 32 km
 29 across the seven models: the
 30 lower part of ≤ 40 km thick
 31 crust (e.g., Missenard et al.,
 32 2006).

34 Setting

35 Morocco lies at the
 36 western end of the Alpine-
 37 Himalayan orogen. The Rif
 38 Mountains in northern Morocco
 39 and Algeria absorb ~ 4.5 mm/yr
 40 of the NNW Africa–Eurasia
 41 oblique convergence, yet
 42 inherited faults in and
 43 lithospheric thinning beneath
 44 the Atlas system localize an
 45 additional 2 mm/yr of intraplate
 46 strain more than 500 km south
 47 of the plate boundary (Azzouzi

48 et al., 2005; Serpelloni et al., 2022). Locally thinned to ~ 60 km, hot and low-viscosity lithospheric mantle beneath the
 49 High Atlas and Anti-Atlas (e.g., Miller and Becker, 2014) responds to far-field compression at a correspondingly high
 50 strain rate, focusing brittle shortening on pre-existing faults in the overlying crust (e.g., Missenard et al., 2006).
 51 Originally formed under Variscan compression or earlier and widely reactivated by Mesozoic rifting (e.g., as



reviewed by Fekkak et al., 2018), these faults control modern structure of the Atlas system as sets of double-vergent thrusts paralleling and bounding the ranges (e.g., Sebrier et al., 2006).

Spatial variations in inherited fault geometry may influence modern shortening directions and strain partitioning (Lanari et al., 2020). Range-bounding thrusts are nearly perpendicular to modern convergence in the HMAJ and oblique to convergence in the WHA (**Figure 1A**); deformation transitions from dominantly reverse faulting with a minor strike-slip component in the HMAJ (El Moudnib et al., 2023) to oblique faulting in the WHA (**Figure 1B**). An increasing contribution from sub-axial (ENE–WSW striking) strike-slip and oblique faults in the WHA accommodates this change: NW to NNW shortening is partitioned between dextral slip on these faults and reverse motion on the ~E–W striking range-bounding thrusts (Lanari et al., 2020).

The Al Haouz earthquake occurred ~20 km south of the south-dipping North Atlas fault and ~30 km north of the north-dipping South Atlas fault. Its nodal planes dip ~30° south and ~70° north. Projecting the trace of the North Atlas fault 20 km southward at 30° dip reaches only 12 km depth at the epicenter. Projecting the South Atlas fault 30 km northward at 70° dip exceeds 82 km depth at the epicenter. Thus, if the Al Haouz earthquake is attributable to either of the range-bounding thrusts, its dip must vary with depth; alternatively, slip may have occurred on a separate fault.

Crustal Stress

Previous Work and Data

Medina (2008) compiled focal mechanisms for all of Morocco. Several earthquakes have moment tensors available from the global CMT project, GFZ-Geofon, USGS, and INGV. No in-situ data are available from the World Stress Map (Heidbach et al., 2016). Most recently, El Moudnib et al. (2023) derived 15 focal mechanisms near the HMAJ, which they combined with several others from the southern Middle Atlas, Eastern High Atlas (EHA), CHA, and areas to the southeast in a single stress inversion. The best-fit tensor favors nearly pure reverse faulting with N–S shortening (the $A\phi$ parameter described below equals 2.51 ± 0.04 , with S_{Hmax} N178E).

This study targets the WHA, some 300 km southwest of El Moudnib et al.’s focus, gathering all 26 focal mechanisms available from -12° to -4° longitude and 28° to 32.75° latitude (**Figure 1**)—no data were available

west of -10° or south of 30°. All 26 have NW- to N-trending maximum shortening directions (the P-axis for reverse to strike-slip events), broadly consistent with regional convergence.

Individual focal mechanisms are poor constraints on the local stress tensor (e.g., McKenzie, 1969), yet several coherent geographic patterns emerge:

- Strike-slip with north-trending P-axes (mean N6W, std 14°; n=9) in the WHA and CHA; the Al Haouz earthquake's reverse component is insignificantly greater than others' (mean rake 12°±30° above horizontal)
- Reverse motions with NW-trending P-axes (mean N39W, std 21°; n=11) in the HMAJ area
- Six strike-slip in the EHA and areas south with mostly NW-trending P-axes.

These patterns will be assessed more critically with formal stress inversions.

Stress Inversions - Approach

Inversions of focal mechanisms for the normalized stress tensor are well established and stem from the axiom that coseismic slip parallels the shear traction on the fault plane (e.g., Angelier, 1979). The best-fit tensor minimizes angular misfits between shear and slip. The normalized stress tensor can be described by the directions of the principal stresses and ratio ϕ :

$$\phi = (S_2 - S_3) / (S_1 - S_3) \quad (1)$$

where $S_1/S_2/S_3$ are the magnitudes of the maximum/intermediate/minimum stress. Simpson (1997) combined ϕ with the style of faulting—normal/strike-slip/reverse—defined by principal axis plunges (following Zoback, 1992) to describe the style of deformation as a quantity $A\Phi$:

$$A\Phi = (n + 0.5) + (-1)^n(\phi - 0.5) \quad (2)$$

with $n=0/1/2$ for normal/strike-slip/reverse faulting. Consequently, $A\Phi$ defines a continuum from radial extension ($A\Phi=0$) to radial contraction ($A\Phi=3$), passing through: normal faulting ($A\Phi=0.5$); oblique extension ($A\Phi=1.0$); strike-slip ($A\Phi=1.5$); oblique shortening ($A\Phi=2.0$), and reverse faulting ($A\Phi=2.5$).

Here, inversions (following Levandowski et al., 2018a) assess uncertainty with 1001 Monte Carlo realizations. Each realization jackknife-resamples (discarding $n_{\text{mechanisms}}^{0.5}$), randomly perturbs the individual slip vectors by $\pm 15^\circ$, and chooses a random coefficient of friction 0.3–0.9. The retained mechanisms are then

iteratively inverted (following Vavryčuk, 2014), selecting the less stable of the two nodal planes for each event with respect to the current estimate of the stress tensor, inverting these mechanisms for an updated stress estimate, and recomputing the stability of each plane, for 5 iterations for each of the 1001 realizations. Values given are the median \pm one standard deviation.

Stress Inversions - Results

The best-fit tensor for the 20 focal mechanisms from the WHA, CHA, and HMAJ area is characterized by oblique compression ($A\Phi=2.12\pm0.11$) oriented $N3W\pm5^\circ$ (**Figure 2A**). The $\sim 20^\circ$ difference between this trend and the NNW convergence direction may reflect the strain partitioning suggested by Lanari et al. (2020). Fit to the mechanisms is acceptable, with 24° average angular misfit between the shear traction on each respective focal plane and the slip vector on the iteratively selected focal plane. A value of $40\text{--}45^\circ$ is often taken as a threshold for homogenous stress (Michael et al., 1990; Michael, 1991).

Including the additional six focal mechanisms from farther east changes results insignificantly (2.18 ± 0.11 , $N10W\pm4^\circ$). To balance the need for sufficient focal mechanisms with sensitivity to stress local to the Houaz mainshock, these inversions weight the individual mechanisms by inverse distance. Furthermore, 7/15 of Moudnib et al.'s (2023) HMAJ mechanisms have rakes of exactly 90° , suggesting they are incompletely constrained (no uncertainties were given), and inverse-distance weighting reduces the influence of these comparatively distal events. Regardless, non-weighted inversions of the 20 WHA, CHA, and HMAJ mechanisms differ insignificantly (2.15 ± 0.03 , $N15W\pm3^\circ$), while those including EHA data show a minor vertical axis rotation (2.12 ± 0.04 , $N22W\pm2^\circ$).

Fault Slip Potential Modeling

FSP modeling quantifies how well faults are oriented for frictional slip in the local stress field. From the 1001 normalized stress tensors, the relative stability of faults can be quantified as functions of orientation—in fact, the inversion algorithm uses normalized instability as the criterion for choosing between the focal and auxiliary planes (Vavryčuk, 2014). To estimate magnitudes of expected destabilizing perturbations, however,

129 1001 full stress tensors are calculated (following Walsh and Zoback, 2016; Levandowski et al., 2018b) at a
130 nominal depth of 25 km, using each of the 1001 inversion outputs and its attendant friction, and sampling average
131 overburden density and pore fluid pressure from uniform distributions 2650 to 2850 kg/m³ and -5 to +5 MPa from
132 hydrostatic, respectively. Then, the shear and normal tractions are computed as functions of fault orientation
133 (strike and dip). Finally, FSP is quantified from the distance from Coulomb failure (dCFS), or difference between
134 shear traction and frictional resistance:

$$135 \quad \text{dCFS} = \text{friction} \times |\text{effective normal traction}| - |\text{shear traction}| \quad (3)$$

136 Because FSP under a given stress depends on fault strike and dip, it complements stress inversions, which
137 treat strike and dip as fixed and minimize misfit to slip vectors (rake). This combination can help to determine
138 focal and auxiliary planes or choose from multiple mechanisms for a single event (Levandowski et al., 2023).

139 For any set of parameters, only two or four fault orientations are optimal (dCFS=0): Examining the
140 median FSP value for each fault orientation across the 1001 calculations, none might appear near failure.
141 Therefore, dCFS is given (**Figure 2B**) as the 90% confidence lower bound: in 10% of Monte Carlo trials, such an
142 increase (or less) would trigger instability on the fault plane in question.

143 In cases of induced seismicity, similar calculations retrospectively find that most events have occurred on
144 faults within ~2 MPa of failure at a nominal depth of 5 km (e.g., Walsh & Zoback, 2016), or ~0.4 MPa/km depth
145 (FSP calculations are primarily sensitive to vertical stress gradients — e.g., Levandowski et al., 2018b). The 90%
146 lower confidence bounds calculated here for the iteratively determined focal planes (black dots in **Figure 2B**)
147 average 11.0 MPa at 25 km nominal depth: 0.44 MPa/km. By contrast, the auxiliary planes (gray dots) average
148 50.6 MPa, or 2.0 MPa/km.

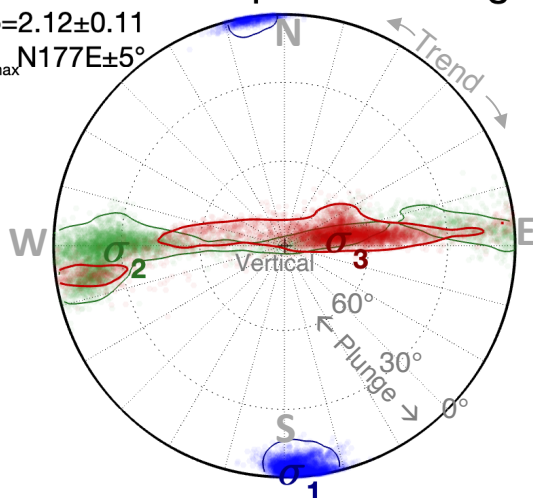
149

A) Stress inversion results

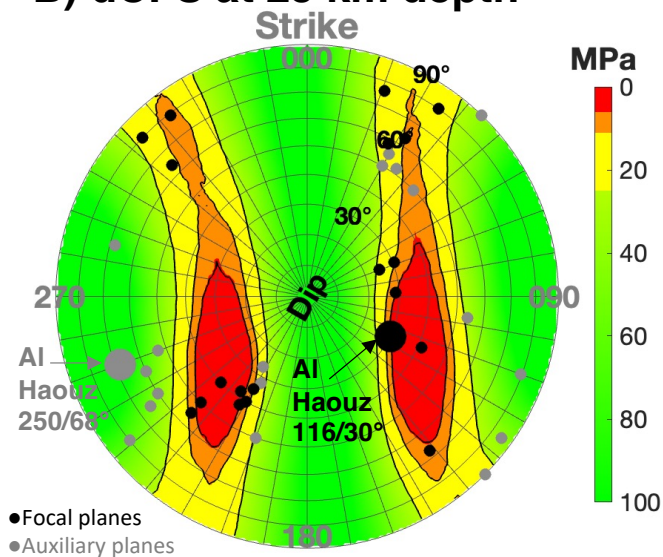
Al Haouz: Oblique shortening

$$A\phi = 2.12 \pm 0.11$$

$$\sigma_{Hmax} N177E \pm 5^\circ$$



B) dCFS at 25 km depth



C) Slip potential of active faults

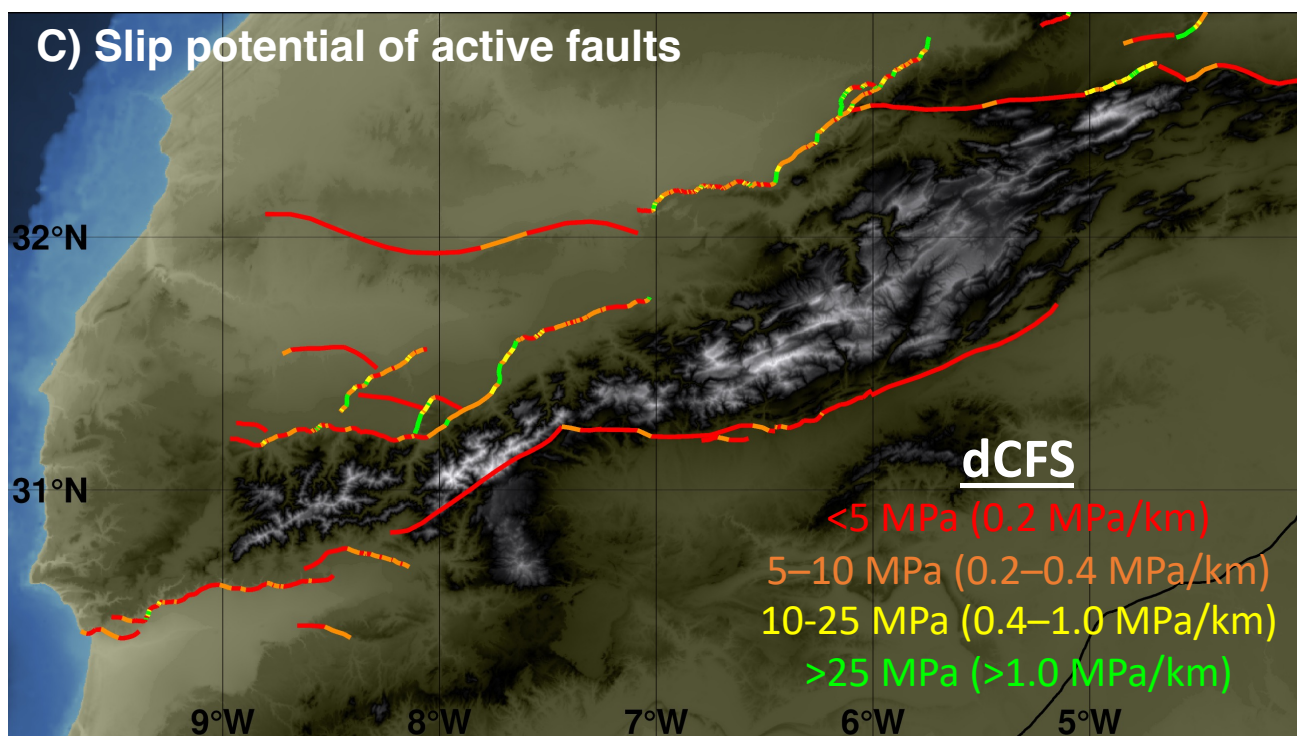


Figure 2: Stress and fault slip potential

A) Stress inversion results Lower hemisphere projection of principal stress axes from 1001 inversions of western High Atlas, central High Atlas, and High/Middle Atlas junction focal mechanisms. The maximum compressive stress (blue) trends

north/south and is sub-horizontal; the minimum (red) and intermediate (green) stresses are of comparable magnitude.

Azimuthal coordinate indicates axis trend; radial coordinate indicates axis plunge.

B) Fault slip potential as a function of fault orientation. Azimuthal coordinate indicates fault strike (as on a compass); radial coordinate indicates fault dip (analogous to axis plunge in lower hemisphere projections such as panel **A**). Values shown are the 90% confidence lower bound of dCFS. Orange and red contours encapsulate the orientations with $dCFS \leq 10$ MPa (0.4 MPa/km), which is a reference threshold for highly susceptible faults taken from induced seismicity (e.g., Walsh and Zoback, 2016). Steep NNE- or SSW-striking faults through gently dipping ($\sim 15\text{--}45^\circ$) E- or W-striking faults, back to steep SE- or NW-striking faults are all near optimal for slip. Black dots: Iteratively selected focal planes of western High Atlas, central High Atlas, and High/Middle Atlas junction mechanisms. Gray dots: Auxiliary planes. Large dots indicate Al Haouz nodal planes; the ESE-striking plane is well oriented for slip ($dCFS=5.3$ MPa) while the WSW-striking plane is not ($dCFS=113$ MPa).

C) Slip potential of active faults from GEM global database (Styron & Pagani, 2020) and Sebrier et al. (2006). Indicated as red and orange traces, most identified fault segments are within 10 MPa of failure at 25 km depth (0.4 MPa/km, which is a typical value for reactivated faults in induced seismicity settings – Walsh & Zoback, 2016).

Active Faults

In regions of mixed modes of faulting, many fault orientations may be suited for frictional slip (Levandowski et al., 2018b). In the WHA, \sim N–S oblique shortening can be accomplished not only by strike slip on steep NE-, SW-, NNE- or SSW-striking fault or by reverse motion on $\sim 15\text{--}45^\circ$ dipping faults striking east/west but also by variably oblique slip on any orientation between (**Figure 2B**). Thus, high FSP (low dCFS) faults form two continua rather than two (reverse and normal) or four (strike-slip) isolated optimal orientations. This diversity notwithstanding, N–S faults of any dip and E–W faults steeper than $\sim 55^\circ$ appear unfavorable.

FSP is next mapped onto known and suspected active faults in the region (**Figure 2C**). The GEM global database (Styron & Pagani, 2020) specifies dip direction and a range of possible dip angles, and additional traces from Sebrier et al. (2006) are digitized and appended. Given the azimuth of each digitized segment, the allowable dip with the highest FSP (lowest dCFS) is selected, and the corresponding dCFS is assigned to that segment. Perhaps not surprisingly, nearly all of the active faults in the region are favorably oriented. Selection of the most favorable dip is justified not only by ignorance of structure at depth but also by the fact that the Atlas faults have been active in two, three, or more events with differing styles, vergences, and degrees of obliquity. In

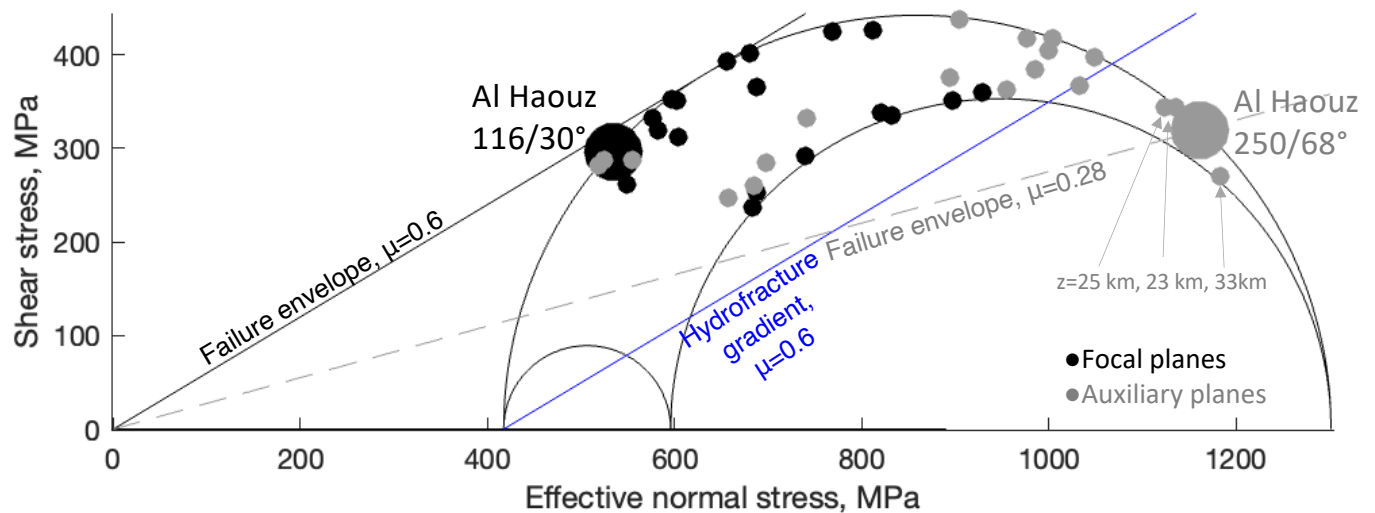
184 intracontinental oblique deformation belts such repeated deformation generally creates bands of sub-parallel faults
185 with varying dips, as individual fault blocks are progressively rotated, and sub-parallel strands coalesce at depth
186 in flower structures (Cunningham, 2013). Indeed, such a mega-flower model is invoked in the WHA (e.g., Ellero
187 et al., 2012). Thus, any given strike at the surface may correspond to a variety of dip angles in the subsurface.
188 Empirically, the selected dips only change by an average 2.3° between adjacent segments of the same fault,
189 suggesting that this treatment does not invoke unrealistic along-strike variations.

190 Haouz moment tensors feature gently south-dipping ESE-striking and steeper north-dipping WSW-
191 striking nodal planes. Finite-fault modeling favors the latter because of superior fit to surface waves (Yeck,
192 written communication 2023— see Acknowledgements), yet stress favors the former in two ways. First, the steeper
193 plane is highly oblique to maximum stress and appears mechanically locked, ~ 375 MPa from frictional failure
194 (**Figure 3**). High fluid pressures alone cannot allow slip on the steep plane because it lies beyond the
195 hydrofracture gradient: Critical pore pressure exceeds the minimum stress, so the rock would fracture before fault
196 slip. Second, and independent of fault instability, the slip vector misfit on the gently south-dipping plane (6°) is
197 lower than that on the steeper plane (24°).

198 Three possible explanations for the different focal plane preferences of the finite fault and stress models
199 include low friction in the hot lower crust, locally anomalous WHA stress, and complex Haouz rupture. Slip on
200 the steep north-dipping plane is mechanically possible if high temperatures (e.g., Missenard et al., 2006) at the
201 lower crustal hypocenter are associated with low fault friction, such as due to partial melt. The Mohr circle in
202 **Figure 3** is constructed for a typical mid/upper crustal friction of 0.6 the focal mechanisms center near 10 km
203 depth except for Al Haouz and three others in the WHA and CHA (23, 25, and 33 km depth)—while the
204 computed shear / normal tractions on the north-dipping Al Haouz nodal plane (325 MPa / 1159 MPa) could
205 destabilize with friction ≤ 0.28 (dashed gray line in **Figure 3**). Low friction does not make this plane less stable
206 than its gently south dipping complement or result in a superior fit between shear traction and slip but does make
207 frictional slip mechanically possible. The same is true for the iteratively determined auxiliary planes for the other
208 three deep WHA/CHA events, all of which are comparatively steep— $231/80^\circ$, $285/68^\circ$, and $110/79^\circ$ —and cluster
209 in the same part of the Mohr circle (**Figure 3**). If low friction is pervasive in the WHA/CHA lower crust, slip on

210 these planes may be permissible. Second, stress could differ in the data-poor WHA from areas to the east with
 211 better constraints. Nevertheless, slip on the ESE-striking plane comports very well with regional stress, both in its
 212 low angular misfit (6°) and low dCFS (~ 0.2 MPa/km: 5.3 MPa at 25 km depth), but additional WHA data will be
 213 needed to determine if this good fit with regional stress is purely coincidental. Finally, a complex rupture—
 214 multiple faults or a non-planar slip surface—could defy assignment of a single focal plane, rendering the
 215 parameterization of the finite-fault model insufficient (Goldberg, written communication 2023—see
 216 Acknowledgements).

217 Regardless, the primary goal of this study is to provide timely information on likely active fault
 218 orientations near Al Haouz, and the result does not hinge on discrimination between the mainshock focal and
 219 auxiliary planes. Slip is favored on orientations from steep NNE-striking through gentle E-striking to steep SE-
 220 striking, and on diametric orientations. Given this unfortunate diversity of susceptible fault orientations, most
 221 mapped active fault segments in the area appear well aligned in the regional stress field.



222
 223 **Figure 3: Mohr Circle** for the single best-fit stress tensor for western High Atlas, central High Atlas, and High/Middle Atlas
 224 junction focal mechanisms and friction, μ , 0.6. Black line: failure envelope for $\mu=0.6$. Blue line: Hydrofracture gradient at $\mu=0.6$.
 225 The WSW-striking Al Haouz nodal plane is beyond the hydrofracture gradient. However, this plane may be compatible with slip
 226 if it has anomalously low friction ≤ 0.28 ; the dashed gray line shows the associated failure envelope.

227

228

229 **Conclusions**

230 Crustal stress in the intraplate High Atlas region—determined by focal mechanism inversions—promotes
231 north-south shortening accomplished a mix of reverse, reverse-oblique, and strike-slip motion. This mixed-mode
232 deformation may reactivate a broad range of fault orientations from steep NNE–SSW-striking to gentle E–W-
233 striking to steep SE–NW-striking planes. This range subsumes most of the known and suspected active faults in
234 the region, suggesting that aftershocks of the deadly M_w 6.8 Al Haouz earthquake and future mainshocks could
235 occur broadly across the inherited fault network.

236

237 **Acknowledgments**

238 The author thanks Dara Goldberg and Will Yeck (USGS) for helpful discussion of the finite fault model.

239

240 **Data and Resources**

241 Focal mechanisms are provided in Table S1. Haouz moment tensors are compiled at [https://emsc-](https://emsc-csem.org/Special_reports/?id=316)
242 [csem.org/Special_reports/?id=316](https://emsc-csem.org/Special_reports/?id=316) (last accessed 25 October 2023). Several of the secondary nodal planes listed
243 there are erroneous; these are corrected—see Table S1—before use in stress inversions. Finite fault model from
244 (<https://earthquake.usgs.gov/earthquakes/eventpage/us7000kufc/finite-fault>, last accessed September 14, 2023).
245 Stress inversion and FSP codes are available at github.com/WillLevandowski/

246

247 **Declaration of competing interests**

248 The author declares no competing interests.

249

250 **References**

251 Angelier, J. (1979) Determination of the mean principal stresses for a given fault population, *Tectonophysics* 56,
252 T17-T26, 1979.

253 Angelier, J. (1990) Inversion of field data in fault tectonics to obtain the regional stress, III, A new rapid direct
 254 inversion method by analytical means, *GeophysJ. . Int.*, 103, 363-376, 1990.

255 Azzouzi, R., M. Ettarid, H. Semlali, A. Rimi, A. Trache, M. Aït Belaid, and L. Aït Brahim (2005). Actual
 256 horizontal displacements and parametric deformation determinations of African and Eurasian tectonic
 257 plates in the Western Mediterranean region. Workshop on Fracture Dynamics: Theory and Applications
 258 to Earthquakes.

259 Cunningham, D. (2013). Mountain building processes in intracontinental oblique deformation belts: Lessons from
 260 the Gobi Corridor, Central Asia. *Journal of Structural Geology*, 46, 255-282.

261 Dziewonski, A. M., T.-A. Chou and J. H. Woodhouse (1981) Determination of earthquake source parameters
 262 from waveform data for studies of global and regional seismicity, *J. Geophys. Res.*, 86, 2825-2852.
 263 doi:10.1029/JB086iB04p02825

264 El Moudnib, L., Timoulali, Y., Nouayti, A., El Abbassi, M., Bouka, M., Nouayti, N., & Mhammdi, N. (2023).
 265 Seismotectonic model of High-Middle Atlas Junction (Morocco) derived from earthquake focal
 266 mechanism and stress tensor analysis. *Modeling Earth Systems and Environment*, 9(2), 2407-2423.

267 Ekström, G., M. Nettles, and A. M. Dziewonski (2012) The global CMT project 2004-2010: Centroid-moment
 268 tensors for 13,017 earthquakes, *Phys. Earth Planet. Inter.*, 200-201, 1-9, doi:10.1016/j.pepi.2012.04.002

269 Ellero, A., Ottria, G., Malus a, M.G., Ouanaimi, H., 2012. Structural geological analysis of the High Atlas
 270 (Morocco): evidences of a transpressional fold-thrust belt. *Tectonics-Recent advances. Intech Open*
 271 *Science*. <https://doi.org/10.5772/50071>

272 Hatzfeld D., Frogneux M. & Girardin N. 1977. Etude de la sismicité dans la région de l'arc de Gibraltar et
 273 l'Algérie du Nord. *Bull. Soc. Géol. Fr.*, (7), XIX, n°4, 741-747.

274 Heidbach, O., M. Rajabi, X. Cui, K. Fuchs, B. Müller, J. Reinecker, K. Reiter, M. Tingay, F. Wenzel, F. Xie, M.
 275 O. Ziegler, M.-L. Zoback, and M. D. Zoback (2018): The World Stress Map database release 2016:
 276 Crustal stress pattern across scales. *Tectonophysics*, 744, 484-498, doi:10.1016/j.tecto.2018.07.007

277 Heidbach, Oliver; Rajabi, Mojtaba; Reiter, Karsten; Ziegler, Moritz, WSM Team (2016): World Stress
 278 Map Database Release 2016. GFZ Data Services, doi:10.5880/WSM.2016.00
 279 Lanari, R., Faccenna, C., Fellin, M. G., Essaifi, A., Nahid, A., Medina, F., & Youbi, N. (2020). Tectonic
 280 evolution of the western High Atlas of Morocco: Oblique convergence, reactivation, and transpression.
 281 *Tectonics*, 39, e2019TC005563. [https://doi.org/ 10.1029/2019TC005563](https://doi.org/10.1029/2019TC005563)
 282 Levandowski, W., Herrmann, R.B., Briggs, R., Boyd, O.S., and Gold, R. (2018a) A revised stress map of the
 283 continental United States reveals evidence for heterogeneous intraplate stress: *Nature Geoscience*, v. 11,
 284 doi:10.1038/s41561-018-0120-x.
 285 Levandowski, W., Weingarten, M., and Walsh F.R. III. (2018b) Geomechanical sensitivities of injection-induced
 286 earthquakes: *Geophysical Research Letters*, v. 45, [doi:10.1029/2018GL077551](https://doi.org/10.1029/2018GL077551)
 287 Levandowski, W., C. Powell, M. Chapman, and Q. Wu (2023). Anomalous Crustal Stress in the Eastern
 288 Tennessee Seismic Zone, *Seismol. Res. Lett.* XX, 1–13, doi: 10.1785/0220220364.
 289 Michael, A. J., Ellsworth, W. L., & Oppenheimer, D. H. (1990). Coseismic stress changes induced by the 1989
 290 Loma Prieta, California earthquake. *Geophysical Research Letters*, 17(9), 1441-1444
 291 Michael, A. J. (1991). Spatial variations in stress within the 1987 Whittier Narrows, California, aftershock
 292 sequence: New techniques and results. *Journal of Geophysical Research: Solid Earth*, 96(B4), 6303-
 293 6319.
 294 McKenzie, D. P. (1969). The relation between fault plane solutions for earthquakes and the directions of the
 295 principal stresses. *Bulletin of the Seismological Society of America*, 59(2), 591-601.
 296 Medina, F. (2008). Catalogue of focal mechanisms of Moroccan earthquakes for the period 1959-2007. ISBN:
 297 9954-8347-9-6 [http://www.israbat.ac.ma/wp-content/uploads/2015/03/03-](http://www.israbat.ac.ma/wp-content/uploads/2015/03/03-%20Medina%20et%20al.%20(19-30).pdf)
 298 [%20Medina%20et%20al.%20\(19-30\).pdf](http://www.israbat.ac.ma/wp-content/uploads/2015/03/03-%20Medina%20et%20al.%20(19-30).pdf)
 299 Miller, M.S., Becker, W.T., 2014. Reactivated lithospheric-scale discontinuities localize dynamic uplift of the
 300 Moroccan Atlas Mountains. *Geology* 42, 35e38.

301 Missenard, Y., H. Zeyen, D. Frizon de Lamotte, P. Leturmy, C. Petit, M. Se'brier, and O. Saddiqi (2006), Crustal
 302 versus asthenospheric origin of relief of the Atlas Mountains of Morocco, *J. Geophys. Res.*, 111, B03401,
 303 doi:10.1029/2005JB003708.

304 Peláez, J.A., M. Chourak, B. A. Tadili, L. Aït Brahim, M. Hamdache, C. López Casado, J. M. Martínez Solares;
 305 A Catalog of Main Moroccan Earthquakes from 1045 to 2005. *Seismological Research Letters* 2007;; 78
 306 (6): 614–621. doi: <https://doi.org/10.1785/gssrl.78.6.614>

307 Serpelloni E, Cavaliere A, Martelli L, Pintori F, Anderlini L, Borghi A, Randazzo D, Bruni S, Devoti R, Perfetti P
 308 and Cacciaguerra S (2022) Surface Velocities and Strain-Rates in the Euro-Mediterranean Region From
 309 Massive GPS Data Processing. *Front. Earth Sci.* 10:907897. doi: 10.3389/feart.2022.907897

310 Simpson, R.W. (1997) Quantifying Anderson's faulting types. *BSSA* 102(B8).

311 Townend, J., & Zoback, M. D. (2004). Regional tectonic stress near the San Andreas fault in central and southern
 312 California. *Geophysical Research Letters*, 31(15).

313 Varryčuk, V. Iterative joint inversion for stress and fault orientations from focal mechanisms. *Geophys. J. Int.*
 314 199, 69–77 (2014).

315 Walsh, F. R. III, & Zoback, M. D. (2016). Probabilistic assessment of potential fault slip related to injection-
 316 induced earthquakes: Application to north-central Oklahoma, USA. *Geology*, 44(12), 991–994.
 317 <https://doi.org/10.1130/G38275.1>

318 Zoback, M. D. (2010). *Reservoir geomechanics*. New York: Cambridge University Press.

319 Zoback, M. D., Townend, J., & Grollmund, B. (2002). Steady-state failure equilibrium and deformation of
 320 intraplate lithosphere. *International Geology Review*, 44(5), 383-401.

321 Zoback, M.L., First and second-order patterns of stress in the lithosphere: The world stress map project, *Jour.*
 322 *Geophys Res.*, 97, 11,703-11,728, 1992.

325 **Supporting Information**

Longitude	Latitude	Depth	Date	Magnitude	Strike	Dip	Rake	Aux Strike	Aux Dip	Aux Rake	Reference
-5.97	31.92	10	2009-07-06	3.6	200	50	-35	314	64	-134	El Moudnib et al., 2023 Event 1
-5.75	32.16	11	2010-08-05	4.3	87	29	119	235	65	75	El Moudnib et al., 2023 Event 2
-6.07	32.36	11	2010-08-05	4.3	114	41	131	245	60	60	El Moudnib et al., 2023 Event 3 duplicate or doublet of Event 2? Martin et al. (2015) 53 36 82 243 54 96
-4.91	32.56	12	2011-05-01	3.3	225	50	50	98	54	127	El Moudnib et al., 2023 Event 4
-5.78	31.95	12	2011-02-14	4.4	35	80	-5	126	85	-170	El Moudnib et al., 2023 Event 5 Martin et al. (2015) 38 84 -4 129 85 -174
-7.32	31.34	13	2011-12-26	3.4	225	55	0	135	90	145	El Moudnib et al., 2023 Event 7 04:33:54; El Moudnib Event 6 (2011-12-16, 04:33:56, Lon -7.29, Lat 31.33, depth 16 km) is clearly a duplicate of this event. El Moudnib et al., 2023 Event 8
-5.53	32.34	8.4	2013-04-27	4.6	215	38	90	35	52	90	El Moudnib et al., 2023 Event 9
-6.26	32.24	9.1	2013-05-27	4.5	69	31	100	237	60	84	El Moudnib et al., 2023 Event 10 08:46:26
-5.39	32.39	7.6	2013-05-31	5.2	212	27	90	32	63	90	El Moudnib et al., 2023 Event 11 14:46:03
-5.38	32.43	5.9	2013-05-31	4.9	70	25	90	250	65	90	El Moudnib et al., 2023 Event 12
-5.34	32.41	13.7	2013-06-25	4.5	208	s	90	28	58	90	El Moudnib et al., 2023 Event 13
-6.2	32.45	5.2	2014-03-12	4.1	210	40	90	30	50	90	El Moudnib et al., 2023 Event 14
-6.18	32.24	5.5	2014-05-12	5.0	225	40	90	45	50	90	El Moudnib et al., 2023 Event 15
-5.6	32.38	6.4	2014-05-19	4.3	210	35	90	30	55	90	Medina (2008) - hybrid solution using Medina & Cherakaoui 1992 and Moreira 1986
-6.06	31.49	33	1967-08-28	4.7	21	76	23	285	68	165	Medina (2008) after El Alami et al. (1989)
-9.62	31.35	25	1988-12-16	NaN	323	79	-170	231	80	-11	Medina (2008) after El Alami et al. (1992)
-9.73	30.41	0.2	1992-04-05	4.7	142	67	139	250	53	29	gCMT
-5.78	32	15	1986-01-28	4.9	212	42	16	110	79	131	USGS, gCMT, GFZ, INGV, IGP, CPPT
-8.391	31.064	26	2023-09-08	6.8	116	30	132	250	68	69	Agadir event from Hatzfeld et al. (1977), compiled by Medina (2008). Other solutions for this event in Medina's (2008) catalog have aberrant E-W shortening
-9.6	30.5	3	1960-02-29	5.9	314	80	180	44	90	10	gCMT / Medina (2008)
-4.32	31.29	5.4	1992-10-23	5.2	187	69	12	93	79	159	gCMT / Medina (2008)
-4.38	31.24	8	1992-10-30	5.1	181	87	18	90	72	177	gCMT 08:39:11
-4.08	32.6	23	2019-11-17	5.08	182	71	7	90	83	161	INGV
-4.55	32.56	10	2018-06-04	4.0	317	72	-161	221	72	-19	INGV 14:39:08
-4.32	32.65	10	2019-11-17	4.54	185	87	-32	277	58	-176	INGV
-4.29	32.72	10	2020-02-16	4.47	19	72	17	284	74	161	

326
327 **Table S1: Focal mechanisms**

328

329

330